Static and fatigue behavior in presence of notches for polyamide 12 (PA12) additively manufactured via Multi Jet Fusion™ process

Andrea Avanzini[1,*], Davide Battini[1], Stefano Pandini[1]

[1] *Department of Mechanical and Industrial Engineering, University of Brescia, Via Branze 38, 25123 – Brescia, Italy*

*corresponding author, andrea.avanzini@unibs.it

ORCIDs: Andrea Avanzini 0000-0002-7188-7687
Davide Battini 0000-0002-2044-5985
Stefano Pandini 0000-0003-2390-8495

DOI: https://doi.org/10.1016/j.ijfatigue.2022.106912

© 2022. This manuscript version is made available under the CC-BY-NC-ND 4.0 license:
https://creativecommons.org/licenses/by-nc-nd/4.0/

ABSTRACT

Static, fatigue and notch sensitivity tests were performed on Multi Jet Fusion™ (MJF) polyamide 12 (PA12) specimens in unnotched conditions or with blunt/sharp notches. Stress concentration factors, and potential applicability of theory of critical distances (TCD) were investigated. Fracture surfaces were comparatively analyzed for quasi-static, fatigue and cryogenic failures. Stress-Life curves were determined and MJF-PA12 showed static and fatigue properties comparable to conventional PA12. The blunt notch had limited impact on fatigue strength, with failure onsetting from internal defects. The sharp notch showed low fatigue notch sensitivity but reduced static strength and fatigue life, with failure onsetting from notch tip.

KEYWORDS

Fatigue; notch; multi jet fusion; PA12; additive manufacturing.

1. INTRODUCTION

Also known as three-dimensional (3D) printing, additive manufacturing (AM) is a general definition that covers different methods used in the manufacturing of 3D objects. AM technologies are continuously evolving and nowadays a variety of processes are available in the market. While Fused Deposition Modelling (FDM) is well-established as a method to produce polymeric parts for rapid prototyping, powder bed fusion (PBF) processes are very promising for the manufacturing of end-use parts in industrial applications [1]. Similarly to other AM technologies, PBF components are obtained through accumulating materials in a layer-by-layer manner. A heat source (e.g., laser and infrared (IR) radiation) is used to build 3D objects parts according to computer-aided design (CAD) model data by melting and coalescing powder particles of a powder bed. Selective laser sintering (SLS) is one of the most established and widely used PBF processes and it uses a laser to selectively sinter thermoplastic polymer powder particles in successive layers [2]. Multi Jet Fusion™ (MJF) on the other hand, is a relatively new technology developed by HP Inc. on the basis of the powder bed fusion (PBF) and binder jetting processes.

MJF does not make use of a laser for powder fusion, but a combination of fusing and detailing agents selectively deposited onto the powder particles in the form of droplets, subsequently scanned with IR lamps across the powder bed to fuse the powder layers in a line-wise manner. More specifically, MJF process consists in coating a build plate with a layer of powder and then depositing a heat-conducting liquid (fusing agent) to increase absorption rate of the infrared radiation of the heating source. In addition, the so-called “detailing agent” is applied around the profile of the desired geometry to prevent melting the raw powder outside the profile thanks to the thermal insulating properties of this liquid. Hence, sharper edges and smoother surfaces can be obtained with tighter geometric tolerances when the (infrared radiation) energy is applied to form a solid layer by melting together only selected powder particles. The process is repeated layer by layer as the build platform moves down and, upon completion, the encapsulated 3D part is removed from the unfused powder and sent to the post processing station to cool down. More detailed descriptions of the MJF process and materials are available in the current literature, see [3–5].

MJF is suitable to produce large quantities of end-use plastic parts with high-quality (comparable or better than SLS) in reduced times. Moreover, MJF allows printing complex and highly overhanging geometries without

CC BY NC ND

the need of support structures and the mechanical properties of printable materials, such as PA12, are within the range of those reported for other production processes [6].

As for SLS, the most used material is the Polyamide 12 (PA12), a semi-crystalline thermoplastic polymer that combines a large processing window, with low density, very good strength, high elongation at break, excellent impact strength and also excellent abrasion and surface slip characteristics [7]. Nowadays, extensive research has been carried out on the chemical, physical, and mechanical properties of PA12 parts printed using SLS, including correlation between processing parameters and tensile properties [8,9], influence of build orientation [10] or multiscale characterization for modelling [11]. Microstructural differences between SLS and injection molded (IM) parts related to different thermal history (i.e. degree of crystallinity, amount of α and γ phases) were also analyzed [12], showing that SLS-PA12 displays good strength, but reduced ductility compared to IM-PA12. It has also been recognized how factors such as porosity or degree of particle melt (DPM) can heavily affect the mechanical performances [13,14].

While according to standard ISO 52900 [15] SLS and MJF are both Power Bed Fusion (PBF) technologies, and thus direct competitors in the market, some differences can still be appreciated since the properties of parts produced by PBF are determined by the building process [16]. In MJF, the cooling is much faster, and the heating of the powder bed is more homogenous, thus reducing the risks of thermal effects, such as shrinking, thanks to the lower temperature gradients and slower heating up of fused areas. Moreover, the consolidation of the polymer powder in MJF is based on the introduction of inks that are not necessary for SLS [17] but the process is much more rapid as it involves the use of line-wise IR radiation treatments, as opposed to the more widely applied point-wise fusion technique [6]. Although commercialization of MJF printers is relatively recent, these differences already motivated specific investigations on MJF-PA12 as well as comparisons with SLS-PA12, mainly considering static mechanical properties.

In [6] the mechanical performance of MJF-PA12 was evaluated with tensile and flexural strength measurements. No significant difference in tensile strength and elastic modulus was observed between the X, Y and Z building orientations defined according to ISO/ASTM 52921, whereas in terms of flexural testing, the build orientations had a significant effect on the strength of the printed part, with samples printed in Z direction featuring a 40% increase in flexural strength. In [17] the morphology, composition and thermal behavior of PA12 powders for MJF were found to be similar to analogous feedstocks for SLS. The tensile

CC BY NC ND

properties of finished parts were generally isotropic, with the exception of deformation at break that noticeably decreased as the loading direction approached the growth direction. In [18], the mechanical properties of SLS specimens were higher than those of MJF specimens, especially Young's modulus and elongation at break and such differences were attributed to the higher density of the SLS specimens. In [19], static tensile tests showed that SLS specimens have a higher Young's modulus than MJF ones but a smaller deformation at break and similar strength. On the other hand, in [3], a comparative study between SLS-PA12 and MJF-PA12 was performed and the tensile strength of the MJF-printed specimens was instead slightly higher than that of SLS-printed ones in each orientation. The higher tensile strength of the MJF-printed parts was deemed to originate from the synergistic effect of the area fusion mode and the reinforcement of carbon black in the PA12 matrix through the fusing agent. Notably, the SLS tensile specimens built along the X and Y orientations had almost the same ultimate tensile strength (*UTS*) and elongation at break (ε_{ab}), whereas the Z orientation presented the weakest tensile strength and ductility. For MJF parts, the opposite behavior was observed, with tensile strength increasing in the sequence of Y, X, and Z orientations, suggesting that the strength across the layers of MJF parts is larger than in SLS part. Limited differences between tensile strengths of specimens built with different orientation were also reported in [20], in contrast with SLS for which Z-orientation usually proved to be the weakest. In [21] a failure criterion with stress interactions for materials with anisotropic properties was proposed to predict failure of MJF-PA12 parts. Coupons were tested under tensile, compressive, shear, and combined loading scenarios. The results showed a significant difference in tensile and compressive strengths, similarly to SLS-PA12. Unlike SLS however, MJF parts did not exhibit a strong interaction between stresses when under combined loading. In conclusion, monotonic properties of MJF-PA12 seem comparable with those of SLS-PA12, but, as can be inferred by the summary of published properties reported [19], the range of values for strength and elastic properties is quite wide.

Considering failure mechanisms, the formation of defects such as voids and imperfections is nearly inevitable during the 3D-printing process. These defects, combined with the resulting layered structure, may lead to anisotropic strength and/or failure modes. Moreover, failure mechanisms can also be different from those of polymers produced with conventional techniques. In particular, [22] suggested the material density being a crucial factor influencing the fatigue life of SLS-PA12 parts. The lower the density, the higher the number of unfused powder particles thus leading to a higher chance of crack nucleation. Pores may also act as stress

CC BY NC ND

concentrators, facilitating crack initiation and failure [12] from material imperfections (i.e. pores) in the specimens rather than from the surface. For MJF-PA12, the presence of defects with diameter of about 1 mm surrounded by non-melted powder was reported in [23].

Besides tensile or flexural properties, knowledge on fatigue behavior and notch sensitivity is also essential, especially when considering the material as a possible candidate for structural applications.

Considering fatigue properties, the few published studies are mostly concerned with SLS-PA12. In [24] high cycle fatigue (HCF) properties were investigated under axial loading with load ratio R = -1 (alternating cycle) and the fatigue limit at 10^6 cycles for plain specimens was estimated at 18 MPa (stress amplitude). In [25] reverse and rotating bending fatigue tests were carried out on SLS-PA12. The fatigue behavior was isotropic and with no statistical difference between rotating and reversed bending fatigue properties, but no estimates of a fatigue limit were provided. Anisotropic response was instead observed for fatigue crack propagation in [26], with worser fatigue performance for specimens tested along the building direction, Z (i.e. the layer plane is perpendicular to the loading direction). The main micro-mechanisms of failure were craze formation, growth and subsequent rupture. Focusing on MJF, some fatigue data were reported by [19] for tests on SLS and MJF cylindrical specimens with pulsating cycles (stress ratio R = 0). However, with a range of maximum applied stress between 32 MPa and 38 MPa, this work only covered a portion of the finite life region of the S-N curve, with failures occurring well below 10^5 cycles in most cases and no run out at 10^6 cycles. The fatigue curve exhibited a distinct knee between 34 and 32 MPa, with higher scatter for MJF than for SLS-PA12. Quite interestingly, in [23] a limit stress for MJF-PA12 was estimated at 29.4±1.6 MPa with a thermographic method. This value was in line with results of fatigue tests on seven specimens, in the range 28-30 MPa with a stress ratio R = 0.1, adopting a number of cycles for run out of N= $2x10^6$. However, as remarked by the author, several traditional fatigue tests should be carried out to obtain the *S-N* curve and the fatigue limit of the material, but to the best of authors' knowledge, this type of data have not been published yet for MJF-PA12.

Considering notch effects, current knowledge is also very limited. An analysis of the notch radius effect in SLS-PA12 specimens under static loading was reported in [27]. The manufacturing direction affected both the value of fracture toughness and tensile strength. Authors investigated the application of Theory of Critical Distances (TCD), reporting that TCD suitably reproduced values of fracture toughness obtained from notched samples of SLS-PA12. In [28] the equivalent material concept (EMC) was used with the J-integral failure

CC BY NC ND

criterion to investigate the failure of the notched samples made of MJF-PA12. While this approach was found to be successful to predict experimental results with numerical models, it must be noted that the properties declared for MJF tensile strength and modulus *E* (34 MPa and 780 MPa, respectively) were significantly lower than those reported by most published works.

Finally, fatigue failure in presence of a notch was investigated for SLS-PA12 only in [22] and [12]. A notch strengthening effect was observed at high load level, with no effect of the built orientation. Fatigue failure was found to be affected by the presence of pores and by interactions between thermal and mechanical damage mechanisms.

In the end, considering the current scientific literature, it is clear that despite the growing interest on MJF-PA12 for industrial applications, both fatigue and notch influence, as well as their combined effects, have not been yet thoroughly investigated. The aim of the present work is to provide new relevant data that could be useful from a design point of view, by investigating fatigue performances and comparing the effects on static and fatigue response of two different types of notches, mild and severe.

2. MATERIAL AND METHODS

MJF-PA12 specimens were provided by ELMEC 3D S.p.A and manufactured with the printer HP – MJF-4200. The PA12 was fed to the printer in the form of powder with a melting temperature, T_m of 187 °C, bulk density of 0.425 g/cm^3 and a particle size of 60 μm.

The specimens were printed flat in the XY horizontal plane, with the Z-axis being the building direction corresponding to the thickness. Specimen types (see Fig. 1) included a dumbbell geometry for tensile tests (as per ASTM D638, type IV) and three different configurations, designated as Smooth, R-notched and V-notched, that were used to investigate notch effects on static and fatigue behaviors. Notched specimens differ for the shape and acuity of the notch, which is far more severe for the V-notched in comparison to the R-notched.

CC BY NC ND

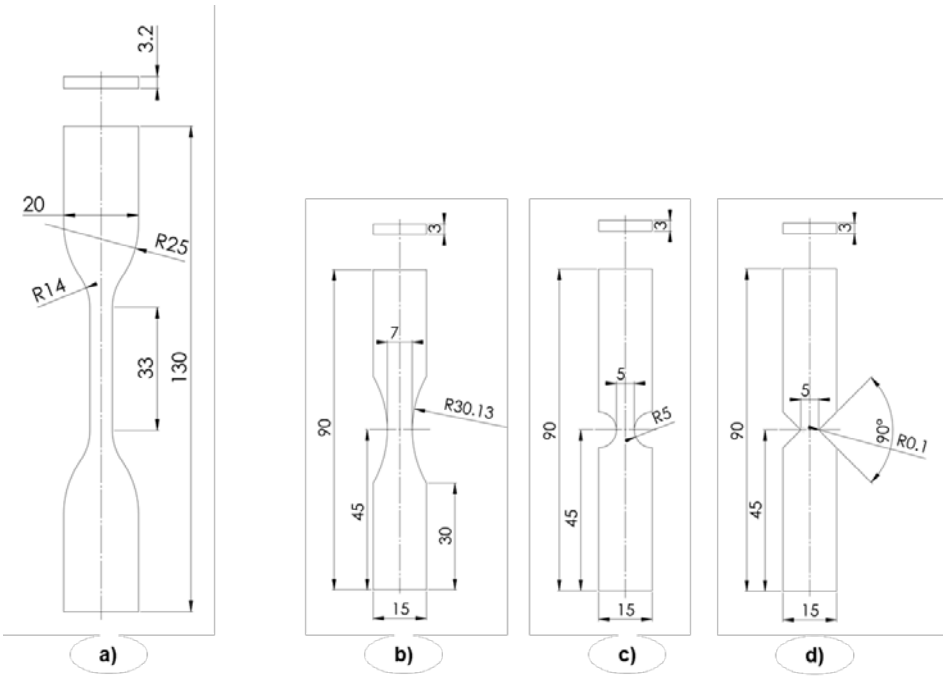

Fig. 1: Specimen geometries for tensile and notch effect tests. a) dogbone specimen, b) Smooth notch specimen, c) R-notched specimen, d) V-notched specimen

The theoretical stress concentration factor K_t associated with each geometry was calculated by means of 2D finite element analysis following the same procedure described in [29,30], as the ratio between peak principal stress and average value in the minimum section when load is applied, assuming linear elastic material behavior and plane stress conditions. The values of K_t were 1.07, 1.31 and 3.82 for Smooth, R-notched and V-notched, respectively. In order to account for slight deviations from nominal to real geometry (especially for very small features), a 0.30 mm notch radius was determined by microscopical analysis for the V-notched specimens. The effective notch radius value of 0.30 mm was thus used for K_t (and any related quantity) calculations in place of the 0.10 mm nominal value.

All the quasi-static tests were carried out on an electromechanical dynamometer (Instron, Mod. 3366). Three specimens with dumbbell geometry were tested with a displacement-controlled configuration, applying a constant crosshead speed of 0.3mm/min and using an extensometer for strain measurement.

For the other geometries, specimens were clamped, leaving a free central region of 40 mm between the grips, and then statically or cyclically loaded. Samples for Smooth, R-notched and V-notched configurations were tested until failure at a crosshead speed of 10 mm/min, recording both the force and the crosshead displacement.

CC BY NC ND

The remaining specimens were used for fatigue tests, which were carried out with a load-controlled configuration on a servohydraulic machine (Instron Dynamight). The test frequency was set to 5 Hz and the stress ratio was set to $R \approx 0.05$ to avoid presence of compression loads. A total of 35 specimens were tested (10 Smooth, 10 R-notched and 15 V-notched), assuming 10^6 cycles as life limit for run out. During the tests, the surface temperature was regularly checked with a contact thermal sensor to detect possible abnormal temperature variations.

Differential scanning calorimetry (DSC Q100 – TA Instruments) and dynamic-mechanical thermal analysis (DMA Q800 – TA instruments) were also performed to identify the glass transition (T_g), melting and crystallization temperature (T_m and T_c respectively), as well as the crystallinity degree (χ_c) of the PA12 after printing. The following parameters were measured: $T_g \approx 43$°C; $T_m \approx 180$°C; $T_c \approx 150$°C; $\chi_c \approx 39$°C (obtained by comparison of the measured melting enthalpy value of 81.8 J/g, to the theoretical melting enthalpy value of 209 J/g for 100% crystalline PA12 [31,32]).

3. RESULTS AND DISCUSSION

3.1. Tensile tests – Dumbbell specimens

Results of tensile tests are reported in Fig. 2 for the dumbbell specimens in terms of nominal stress-strain curves, together with values of tensile modulus, *E*, ultimate tensile stress, *UTS*, and strain at break, ε_{aB}. Compared to the values of the tensile properties declared by the manufacturer of the 3D printer [33], the specimens displayed a similar average elastic modulus (1640 ± 31 vs 1700 MPa), but slightly lower average ultimate strength (43 ± 2.7 vs 50 MPa) and average strain at break (10% ± 3.4 vs 17%).

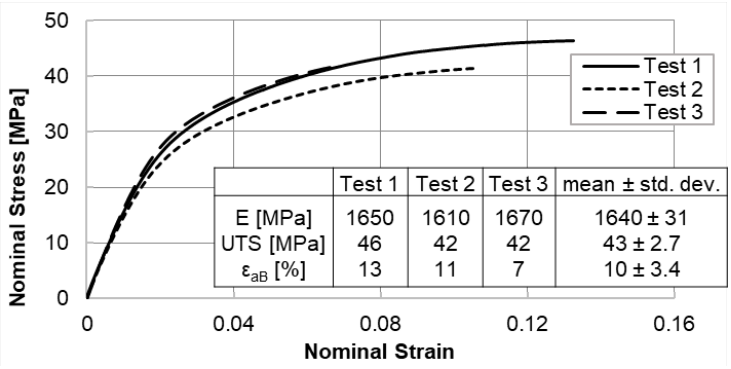

Fig. 2: Results of the tensile tests on dumbbell specimens.

According to the manufacturer [33], tensile strength typical variation (95% of parts) should fall within the 45-55 MPa range, while tensile modulus values should remain within the 1500 to 2100 MPa range. The findings of the present study lie within these intervals, but the range of these properties seems actually even larger when considering published data, as indicated by the summary in Tab. 1.

Such discrepancies are somewhat to be expected, as the experimental measurements are heavily influenced by the testing conditions and the final part properties are strongly related to the printing process parameters. As observed in [18] while SLS has been well developed for several decades, making its processing parameters definition quite mature and well optimized, MJF is still an emerging technology and optimal processing parameters are still under development.

UTS (MPa)		E (MPa)			
Average	Std. dev.	Average	Std. dev.	Build Dir.	Ref.
41.24	1.18	-	-	XY, X	[21]
48.97	1.01	-	-	XY, Y	[21]
34.91	-	780	-		[28]
50	-	1700	-	XY	[33]
50	-	1900	-	Z	[33]
39	-	-	-	Z	[17]
36	-	-	-	XY	[17]
32.0	5.5	1560	5.5	Z, milled	[17]
37.5	2.3	1370	17	XY, milled	[17]
45.6	0.4	1530	60	Z	[19]
40.10	1.49	1420	40	XY	[18]
47	0.9	1242	28	X	[6]
48	0.8	1147	28	Y	[6]
49	0.6	1246	37	Z	[6]
48.7	0.8	1369.0	25.0	X	[3]
44.5	0.7	1368.8	97.6	Y	[3]
49.6	1.2	1669	66.7	Z	[3]
45.7-53.0	-	1408-1688	-	XYZ, ZXY	[20]
49.9	1.9	3940	360	X	[34]
49.3	3.4	3970	310	Y	[34]
48.7	0.8	1370	30	Z	[34]
45.8	3.5	1128	68	X	[35]
47.9	0.9	1204	84	Y	[35]
53.7	1.1	1337	98	Z	[35]
45.15	-	-	-	Y	[36]
47.77	-	-	-	Z	[36]

Tab. 1: Tensile properties of MJF PA12 from current literature.

From a design perspective, the stress-strain curve also provides essential information for the choice of a constitutive model. The response of MJF-PA12 under quasi-static tensile loading is similar to that of other thermoplastics polymers, with a smooth transition from the initial elastic response to irreversible plastic deformation and no clear yield point. This type of stress-strain response can be conveniently fit with a Ramberg-Osgood type of relationship as per eq. (1):

CC BY NC ND

$$\varepsilon = \frac{\sigma}{E} + \left(\frac{\sigma}{H}\right)^{\frac{1}{n}} \quad (1)$$

in which n is a strain hardening exponent and H is an additional constant that can be determined following the procedure outlined in [37] and based on a linear regression of the logarithms of stress and plastic strain. As shown in Fig. 3, an excellent fit (R^2 =0.998) of experimental data for test 1 was obtained with the following values: n = 0.228, H = 91.81 MPa and E = 1650 MPa.

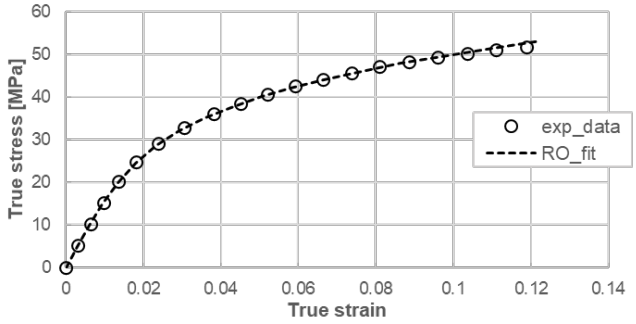

Fig. 3: Fitting of MJF-PA12 tensile stress-strain curve with Ramberg-Osgood equation, eq. (1).

While Ramberg-Osgood equation can be useful when developing analytical models, as for example for the study of notch behavior in presence of plasticity, it has to be remarked that this approach is purely phenomenological. A more detailed constitutive modelling of thermoplastic polymers remains challenging and requires the use of advanced visco-plastic laws to account for both the viscous and the plastic contributions. Ideally, for additively manufactured polymers such models should also take into account anisotropic effects and asymmetric behavior in tension and compression [38]. For SLS-PA12 attempts in this directions have already been presented in [39], where the strain rate-dependent behavior was simulated numerically comparing visco-plastic material models of Chaboche and Bodner-Partom, and in [40], where the so-called Three Network (TN) material model was considered. In practice, theoretical development, numerical implementation and definition of test procedures for material parameters determination is a difficult task, although a finite-strain viscoelastic-viscoplastic constitutive model based on the logarithmic stress rate was recently developed in [41] for the matrix of MJF PA12.

3.2. Tensile tests – smooth and notched specimens

Results of tensile tests on smooth and notched specimens are reported in Fig. 4, in which the nominal stress was determined as the ratio between applied load and the minimum net section area. It must be noted that while

CC BY NC ND

specimens were gripped by keeping the same distance between the clamps, the minimum cross-section of the Smooth specimen (21 mm^2) was larger than the one of the notched specimens (15 mm^2, for both notches). Interestingly, the presence of the notch affects the overall behavior of the tested specimens, with crosshead displacement at break of the Smooth specimens being higher than that of the R-notched and V-notched ones. Comparing *UTS*, the Smooth specimens broke at ≈ 50.9 MPa average, a slightly higher value than dumbbells but still within the expected range. For R-notched specimens *UTS* was instead ≈ 46.9 MPa whereas for V-notched a value of ≈ 39.5 MPa was identified. In this regard, one should note that the *UTS* of the smooth specimens was slightly higher than the one obtained from dumbbells specimens. While direct comparison might not be so straightforward because of the different geometries, MJF can exhibit (as recently reported in [41]) some sensitivity to strain rate effects and this discrepancy could be related to the different testing conditions, with tests on smooth samples being relatively faster.

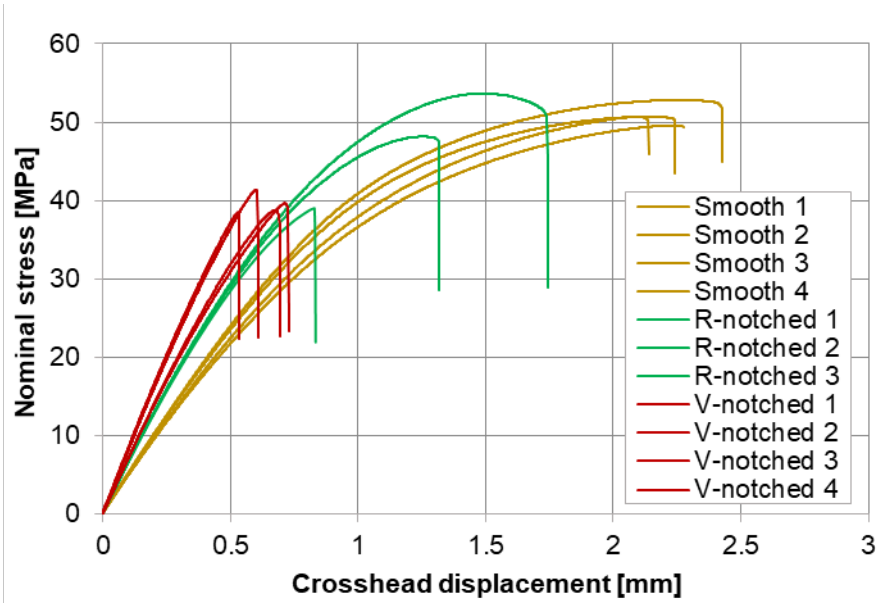

Fig. 4: Results of the tensile tests on Smooth, R-Notched and V-Notched specimens

Considering that the K_t value for Smooth specimens was close to 1, this specimen geometry can be considered an approximate representation of the un-notched condition, as also indicated by the fact that its *UTS* was even higher than the one dumbbell tests. An experimental notch factor at failure under static loading, K_{st}, can thus be estimated as per eq. (2):

$$K_{st} = \frac{UTS_{smooth}}{UTS_{notched}} \tag{2}$$

CC BY NC ND

This resulted in K_{st} = 1.09 for the R-Notched and K_{st} = 1.29 for the V-notched, with the former being closer to its theoretical K_t value of 1.31 while the latter being significantly lower (V-notched K_t = 3.82).

Considering the severe 0.3 mm tip radius of the V-notched specimens, the ductility of the material may have helped by redistributing the high peak stress over a small area ahead of the tip, resulting in an experimental notch factor for static failure K_{st} much lower than the theoretical K_t. For the round notch this effect was less noticeable because the notch is less severe and causes smaller stress gradients.

While there are no investigations on notched MJF-PA12, it should be noted that findings of the present work are only in partial agreement with those reported in [12] in which SLS-PA12 and IM-PA12 notched specimens reached higher *UTS* than the unnotched specimens. This notch strengthening effect was attributed to an increasing load carrying capacity of the notched area after local yielding. According to [12], the increasing stress induced voids nucleation in the localized plastic zone near the notch, eventually leading to crazing and macroscopic brittle failure perpendicular to the loading direction. In the present work, *UTS* of notched specimen was closer than theoretically expected to *UTS* of un-notched specimens, but not higher and it was not possible to assess the presence of crazing. On the other hand, it should also be noted that the V-Notched specimen geometry differs a lot from the one tested in [12] making a direct comparison quite complex.

The analysis of the response in presence of different notch geometries also allows some preliminary considerations on a possible application of the theory of critical distances (TCD) to MJF-PA12. The TCD is a group of theories which use a common critical distance, *L*, to assess the local stresses ahead of a stress concentrator apex. The TCD has been formalized into four methods which include the Point Method (PM), the Line Method (LM), the Area Method (AM), and the Volume Method (VM) [42]. As observed in [43], while the volume method and the area method represent very elegant formalizations of the TCD, in practice their use is more cumbersome, whereas line and point method greatly simplify the practical application of TCD. In particular, using the PM is relatively easy for notched parts under tensile loads and several examples of its application are reported for different 3D printed polymers in the current literature [27,44–47]. For the PM method, the mathematical definition of *L* is given in eq. (3):

$$L = \frac{1}{\pi}\left(\frac{K_{IC}}{\sigma_0}\right)^2 \tag{3}$$

where σ_0 is the so-called materials inherent strength, which may be higher than *UTS*, and K_{IC} is the plane strain fracture toughness. According to PM method for example, failure will occur when the stress at a critical

CC BY NC ND

distance *L/2* reaches the value σ_0 [48]. TCD parameters *L* and σ_0 are usually determined experimentally for each material. For example, one can plot the critical stress-distance curve in the incipient failure condition for two geometric configurations containing different stress concentration features.

For the present case, R-notched and V-notched were assumed as blunt and sharp configurations respectively and their stress-distance curves were determined by means of a 2D FEM model assuming a linear elastic behavior and a plane stress formulation. Results are reported in Fig. 5 and led to a *L/2* estimate of 0.379 mm whereas σ_0 was 50.4 MPa.

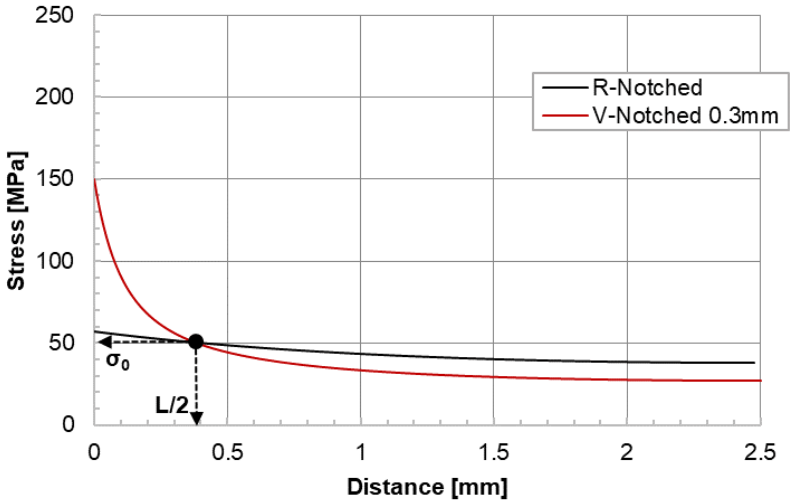

Fig. 5: Linear elastic stress-distance curve in the incipient failure condition. Chart used for the determination of the TCD parameters σ_0 and *L/2*.

Of course, in order to validate TCD applicability, further tests should be carried out on specimens with different notches, to check whether the failure loads predicted with TCD are coherent with experimental results. Quite interestingly, following [49] by rewriting eq. (3) as per eq. (4), the plane strain fracture toughness can also be determined as:

$$K_{IC} = \sigma_0 \sqrt{\pi L} \tag{4}$$

With the TCD parameters previously determined, for MJF-PA12 under investigation, a value of K_{IC} of 2.46 MPa√m can be calculated. Unfortunately, it is not yet possible to directly compare this result with experimental studies on fracture toughness of MJF-PA12, since to the best of the authors' knowledge such data is not available in current literature and performing similar investigations was beyond the purpose of the present work. However, some data is available for SLS-PA12: a K_{IC} value of 3.2±1.2 MPa√m was reported in [50], whereas for samples printed in XY, K_{IC} was in the range 2.182-2.902 MPa√m in [51]. Despite the variability

CC BY NC ND

of these results, considering the similarities between SLS and MJF, the predicted value seems to fall within a plausible range. Of course, further research is certainly needed, concerning both different notch geometries and direct experimental testing of MJF-PA12 fracture toughness.

In the end, it is worth remembering that an analysis of the notch radius effect in SLS PA12 specimens was presented in [27], together with the application of the PM TCD, with a successful experimental validation of their apparent fracture toughness obtained via fracture tests with sharp crack specimens.

In conclusion, it should also be remarked that results of the present study refer to samples printed flat in the XY plane and further investigations are needed to assess TCD parameters and notch effect for different printing directions. Moreover, in a recent paper [52], the effects of changing specimen orientation for a given building direction were also investigated. While the results showed that MJFPA12 is not sensitive to planar orientation when specimens are printed flat (as in our study), this so-called secondary orientation may affect properties for the other printing directions.

3.3. Fatigue life curves

The experimental data obtained for the three families of specimen tested are summarized in Fig. 6, in the form of a traditional log-log S_{max}-N_f curve, with S_{max} being the peak stress of the loading cycle and including run-out at 10^6 cycles.

CC BY NC ND

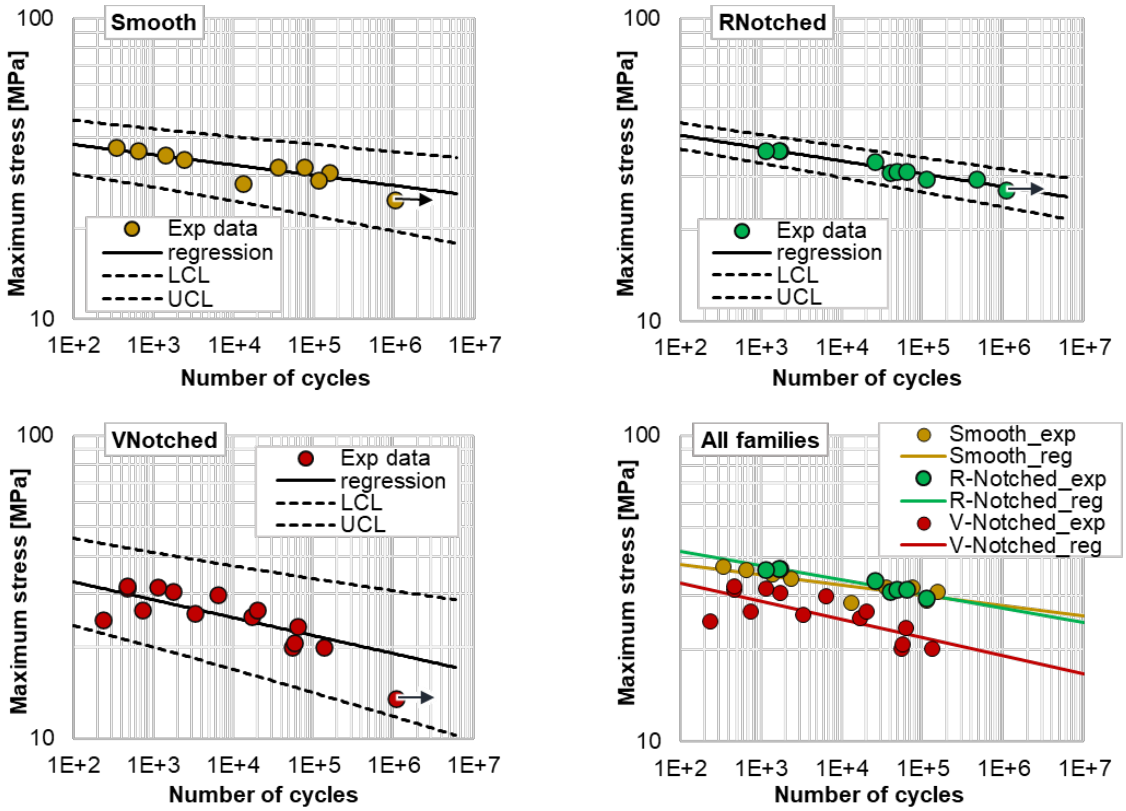

Fig. 6: Fatigue life (S-N) curves with regression as per eq. (5). a) Smooth specimens; b) R-Notched specimens; c) V-Notched specimens; d) All families. a), b) and c) also include upper and lower confidence limits at 90% confidence level (UCL and LCL respectively).

Similarly to what prescribed by Standard ISO 12107 for metallic materials, the experimental stress-life data were processed and a linear regression of the number of cycles to failure, N_f, vs. the maximum applied stress, S_{max}, was carried out in log-log coordinates. Specifically, fatigue data were fit with the Basquin-like power law equation (5):

$$S_{max} = A\left(N_f\right)^B \tag{5}$$

where, A and B are constants, which were in fact determined through linear regression of the experimental results in the finite life regime via eq. (6):

$$\mathrm{Log}(S_{max}) = \mathrm{Log}(A) + B\,\mathrm{Log}\left(N_f\right) \tag{6}$$

Ideally, further tests should be carried out in the infinite life region to determine the fatigue strength with the staircase method. However, applying the staircase method to achieve an accurate fatigue strength identification would require a much higher number of specimens and much longer tests due to the low frequency chosen to avoid self-heating issues. For this reason, a fatigue strength was instead estimated from equation (5) as the S_{max}

associated with 10^6 cycles (N_f) to still allow for some additional fatigue notch sensitivity considerations. In particular, the estimated fatigue strength at 10^6 cycles for the Smooth specimen was 27.7 MPa, whereas for R-notched and V-notched specimens the values were respectively 27.8 MPa and 19.1 MPa.

Results are summarized in Tab. 2, which also includes the applied peak stress S_{max} for the specimens that ran-out after 10^6 cycles and the scatter index at 10^6 cycles, T_{10^6} (defined as the load ratio between the upper and lower confidence limit at 10^6 cycles). Evidently, the stress that the Smooth specimens could withstand for 10^6 cycles was very close to the 28-30 MPa range predicted in [23] for tests with a stress ratio R = 0.1. This result shows that the estimated fatigue strength of this class of 3D printed materials can be surprisingly high even in comparison with thermoplastic semicrystalline polymers manufactured with conventional methods, despite the possible presence of defects inherently created by the layer-by-layer processing.

	B ± std.dev.	A ± std.dev.	S_{max} for 10^6 cycles: ran-out specimens	Estimated fatigue limit (MPa) at 10^6 cycles from eq. (5)	Scatter index at 10^6 cycles, T_{10^6}
Smooth	-0.034 ± 0.0087	44 ± 3.62	24.8	27.7	1.84
R-Notched	-0.042 ± 0.0042	49.9 ± 2.11	27.1	27.8	1.34
V-Notched	-0.06 ± 0.014	43 ± 5.64	13.5	19.1	2.60

Tab. 2: Fitting parameters and peak stress at 10^6 cycles for the fatigue life curves as per eq. (5).

Overall, comparison with data available for SLS-PA12 is less straightforward because the few published data refer to different test conditions in terms of load ratio, specimen shape and frequency. As a reference, tension-compression tests on cylindrical specimens were performed in [22] and a clear fatigue limit was identified: at 10^6 cycles, all specimens endured stress amplitudes of at least 18 MPa, with limited differences between plane Injection Molded and plane SLS specimens. In [25] reversed and rotating bending were considered but the fatigue life curve were provided without a fatigue strength estimate.

Finally, considering the testing condition of the present work ($R \approx 0.05$), some cyclic creep with a progressive shift of the stress-strain cycle during the test along the strain axis was observed, as typically occurs when polymers or polymeric matric composites undergo cyclic load loading with a non-negligible mean stress [53,54]. Although the effects of mean stress on fatigue were not specifically investigated in the present study, it is worth noting that some investigations can be found in literature for polymers and their composites. In [55], different thermoplastics were tested under fatigue with different load ratios, showing a pronounced effect of

CC BY NC ND

mean stress. The possibility to apply mean stress equation corrections was also investigated, highlighting some limitation of typical approaches developed for metal fatigue. In [56], for PEEK composites the effect of tensile mean stress was more pronounced in the LCF regime compared with the HCF regime, with small or no difference in fatigue lives between R= 0.1 and R= 0.3. This was attributed to increased dependence of fatigue behavior to the maximum stress and yielding in low cycle fatigue regime, in addition to the stress amplitude. More specifically for AM polymers, in [57], an investigation of the detrimental effect of superimposed static stresses on AM PLA's fatigue strength was carried out, leading to the suggestion to handle the design problem in terms of maximum stress in the cycle, eventually referring to a unifying design curve in the absence of specific data.

3.4. Fatigue notch sensitivity

Considering the notch sensitivity, two distinct outcomes were observed. The fatigue behavior of R-notched specimens was actually very similar to that of Smooth specimens, both considering the slope of the S_{max}-N_f curve and the estimated fatigue limit at 10^6 cycles, which was almost equivalent, despite the difference in terms on theoretical K_t value (1.31 for R-notched vs. 1.07 for Smooth specimens).

On the contrary, in presence of a sharper notch (i.e. the V-notched geometry), a substantial reduction of the fatigue strength could be observed. As for static tensile tests, the effective influence of the stress concentration determined by the notch were evaluated from experimental data by comparison with Smooth specimens, assuming again that they represent a reasonable approximation of the un-notched condition. In particular, the fatigue notch factor K_f was thus calculated as per eq. (7):

$$K_f = \frac{S_{max,10^6,smooth}}{S_{max,10^6,notched}} \tag{7}$$

which resulted in K_f = 0.996 for R-notched specimens and K_f = 1.450 for V-notched ones. An estimate of the effect of a notch with a given size and shape on the fatigue properties of a material can then be provided by defining fatigue notch sensitivity as per eq. (8):

$$q = \frac{K_f - 1}{K_t - 1} \tag{8}$$

A material is said to be fully notch sensitive under fatigue if q approaches a value of 1.0 while it is not notch sensitive if the ratio approaches zero. For a given material, q increases with notch radius, and within a given

CC BY NC ND

class of materials, q increases with ultimate tensile strength [37]. In general, the discrepancy between K_f and K_t is higher for strongly ductile materials and sharp notches, and lower for more brittle materials and blunt notches. For the examined configurations, the R-notched has a notch sensitivity close to zero, whereas a value of 0.159 can be estimated for the V-notch. It should be underlined that these values were determined by considering the fatigue limit estimated at the highest cycle number within the experimental range of the fatigue life curves (10^6 cycles). Considering the different slopes of smooth and notched specimens, different values may be found for higher cycles number, but further tests should be carried out to properly investigate this aspect. The value of q being almost zero for R-notched specimens actually reflects the fact that for this geometry there is very little difference with the smooth specimen in term of fatigue resistance. Interestingly, for specimen geometries very similar to those used in our studies, but different AM materials, different values of q were reported in literature. As an example, if considering different AM materials, the current literature reports different values of q for specimens with very similar geometries to those used for our study. As an example: in [58] a titanium alloy additively manufactured with DED was tested and the fatigue notch sensitivity was close to zero; in a previous study on a SLM CoCrMo alloy we found q = 0.4-0.54 depending on heat treatment; and in [59], for SLM Inconel 718, a value higher than unity was even reported.

These results suggest that the values for fatigue notch sensitivity do not describe the material properties, but rather a combination of material and "component" properties, including geometrical effects from the build as also remarked in [59]. It can thus be argued that, when considering the competition between geometry and local defects generated by the AM process, these latter could be stronger mechanisms for fatigue failure than global notch geometry if the notch is not severe enough.

Overall, when considering polymers, it should be noted that very little information is available concerning this point even if these relatively low q values are in line with the ductile nature of the material. As a reference, for a PP used in the automotive industry a value of 0.34 was reported in [60], for specimens with a hole and subjected to axial loading. In that study, it was also observed a lower notch sensitivity in the low cycle fatigue (LCF) region as compared to the high cycle fatigue (HCF) regime. This difference was attributed to the fact that at positive R-ratios the maximum stresses were close to (or even above) the yield strength of the material. Therefore, different failure mechanisms may be dominant in different regions, with yielding playing a dominant role in fatigue failure in LCF, whereas at low stresses (HCF) crazing can play a dominant role.

CC BY NC ND

Considering the present work, the steepest slope of the V-notched fatigue life curve in comparison with the Smooth and R-notched ones suggests that a similar effect may be present, although data for this family are more dispersed than for Smooth and R-notched. It should also be remembered, that considering SLS-PA12, a partially different behavior was reported in [12,22], where the fatigue resistance at 10^6 load cycles of notched and un-notched samples converged to a similar value, whereas the notched samples showed improved fatigue resistance with respect to the plain samples in the region between 100 and 10^5 load cycles. This behavior was associated with the low stress amplitude required in the $10^5 \div 10^6$ cycles region causing the same failure mechanism (related to mechanical load only) for both plain and notched samples. Cracks nucleated from unmolten powder particles inside the specimen and hence the peak stress caused by the geometrical stress raiser did not influence the mechanical failure. Such a load dependent notch-strengthening effect is indeed similar, though less evident, to the behavior observed for R-notched samples in the present work. A different behavior was observed instead for the V-notch, suggesting that if the notch is sharp enough, fatigue failure may be controlled by the stress gradient in the notch region rather than by the defects of the additively manufactured material.

As previously done for static loading, a preliminary assessment of the applicability of TCD to fatigue of notched components was also considered. The application of TCD to fatigue problems assumes that fatigue damage depends on the stress field distribution in the vicinity of the stress concentrator. Accordingly, eq. (9) shows that notched components are in their fatigue limit condition when the effective stress, $\Delta\sigma_{eff}$, which depends on the entire stress field distribution ahead of the tip of the stress concentrator, is equal to the material plain fatigue limit, $\Delta\sigma_0$:

$$\Delta\sigma_{eff} = \Delta\sigma_0 \tag{9}$$

Different definitions of $\Delta\sigma_{eff}$ were proposed in literature. Considering the PM method, and following [61] one possible formalization is:

$$\Delta\sigma_{eff} = \Delta\sigma_1\left(\theta = 0, r = \frac{L}{2}\right) = \Delta\sigma_0 \tag{10}$$

In which $\Delta\sigma_1$ is the range of the maximum principal stress and polar coordinates, θ and r, are defined as per Fig. 7.

Regarding the V-notched specimens, a load of 292 N was calculated as corresponding to its estimated fatigue limit of 19.1 MPa. By applying this load to the previously used FE model, the corresponding $\Delta\sigma_{eff}$ resulted

CC BY NC ND

25.5 MPa at a *L/2* distance from the notch root. According to eq. (10), this should also be equal to the material plain fatigue limit, for which the experimental value is instead 27.7 MPa (see Tab. 2). By comparing the two values of $\Delta\sigma_0$, the TCD prediction is thus about 8% lower than experiments, well within the error interval of about 20% which is usually assumed as a reference for TCD predictions to account for variability of fatigue data [61].

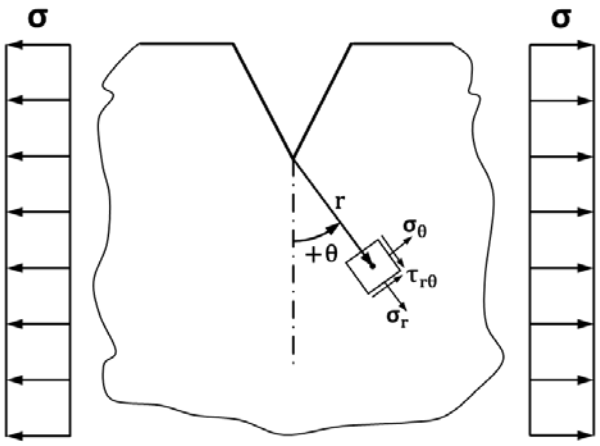

Fig. 7: Notched specimen subjected to a remote uniaxial fatigue loading and polar coordinates system (adapted from [61]**).**

3.5. Fatigue failure mechanism

The failure surface of various specimens, fractured under different conditions, were observed at the optical microscope (Leica DMS300) to investigate the mechanisms dictating failure of the specimens tested in the present work. Cryogenic fractures of the untested specimens were realized to reveal the internal structure of the specimen by fracturing it in the most brittle (or least plastic) conditions.

Fig. 8 shows five different fracture conditions for each specimen family: Smooth, R-Notched and V-Notched. In all cases, the presence of voids could be noticed, and the layered structure was clearly visible.

3.5.1. Fracture surface generated on untested specimens by impact after immersion in liquid nitrogen (cryogenic conditions, Fig. 8a)

For the V-notched specimens, as one can expect, failure occurred in a brittle manner, on a single fracture plane, revealing the evident presence of voids and printing layers. By contrast, the surfaces of Smooth and R-notched specimens revealed a failure surface that was not so severely interested by brittleness despite the harsh conditions. A less planar surface, with respect to V-notched specimens, was generated with significant

CC BY NC ND

deviation from the fracture plane (in particular regions contoured by the dashed line), a reduced presence of holes and slight evidence of layers, suggesting an inherent tougher mechanical response for these types of specimens and notches.

3.5.2. Fracture surface generated under static conditions (Fig. 8b)

The specimens failed under static conditions did not display any sign of plastic deformation mechanisms, neither considering the stress-strain curve nor from the fracture surface morphology, consistently with the small displacement at break. The fracture surfaces show the presence of a flat region, located at one of the borders, (or at both borders in the case of the V-notched specimens), that seems slightly brighter than the rest, and a remaining rougher one. This suggests a failure occurring as a process generated by defects located at specimen borders and rapidly propagating in the inner region.

3.5.3. Fracture surface generated under fatigue conditions at the maximum stress (i.e. low cycle fatigue, Fig. 8c), and at the minimum stress explored (i.e. high cycle fatigue, Fig. 8d)

The fracture surface of specimens failed under fatigue seems to suggest a more extended mechanism than what observed under static conditions. In fact, the planar fracture surface extended even more with respect to static loading. By visually inspecting the specimen appearance during the fatigue test, no signs of crack formation were observed until the last few cycles, when the planar zone generates as early failure process; then, in few more cycles the rougher zone appears, rapidly causing the final failure. The early cracked zone clearly evidenced the presence of holes and of the layered structure, suggesting that fatigue failure at the various loads originated from these types of sub-critical defects, and in particular close to the specimen borders. The rougher region, related to the faster propagation occurring once the main defect has reached critical size, closely resembles those generated under cryogenic fracture conditions. Again, Smooth and R-notched specimens showed similar fracture surfaces, consistently with the similar fatigue strength, where the early failure process seemed to originate from the outer surface, while in V-notched specimens the first fracture stage apparently onsets at both the notch tips. No significant differences were shown, for each family, when comparing failure under the maximum and minimum stress, although, reasonably, for this latter condition the planar region looked slightly larger in the case of the minimum stress, and the rough region more confined, supporting the idea of a larger propagation failure of sub-critical defects under lower stress condition.

CC BY NC ND

3.5.4. Fracture surface generated, in cryogenic conditions, on specimens tested by fatigue and survived to at least 10^6 cycles, Fig. 8e

Finally, cryogenic fracture was carried out also on specimens that did not show failure in the early 10^6 cycles, with the aim of potentially revealing the presence, if any, of damaging mechanisms that took place during fatigue test and cumulated in the specimens. Interestingly, fracture surfaces resulted similar to those of unfailed specimens, suggesting that the cumulated damage is negligible or at least much lower than the amount preceding fatigue failure.

Of course, because of the viscoelastic behavior of polymers, the self-heating induced by cyclic testing conditions can also influence fatigue strength in a complex way [62,63]. In general, an increasing specimen temperature may lead to a deterioration of the fatigue behavior [64] and to a stiffness degradation for polymers with low glass transition temperature. However, as observed in [12], the temperature increase may also delay fatigue failure initiated from pores and subsequent micro-voids coalescence, by inhibiting crack nucleation and propagation thanks to local melting, increased elasticity of the chains or alterations of crystal structure.

Overall, the performed thermo-mechanical characterization of MJF-PA12 confirmed that particular attention should be paid to self-heating effects during fatigue tests as its glass transition temperature was measured at 43°C, thus being very close to ambient temperature and likely leading to a highly hysteretic fatigue response. However, for the present investigation, surface temperature never raised more than 3-5°C, and this was only observed on the Smooth specimens at the highest stress amplitude. In fact, no sudden variations of the stiffness, possibly related with self-heating were observed. This suggests that specimens testing conditions were far from those that may lead to thermal failure. However, it must be noted that discerning between the simultaneous effects of temperature and damage occurring as a consequence of cyclic loading, is especially challenging in presence of notches [65].

CC BY NC ND

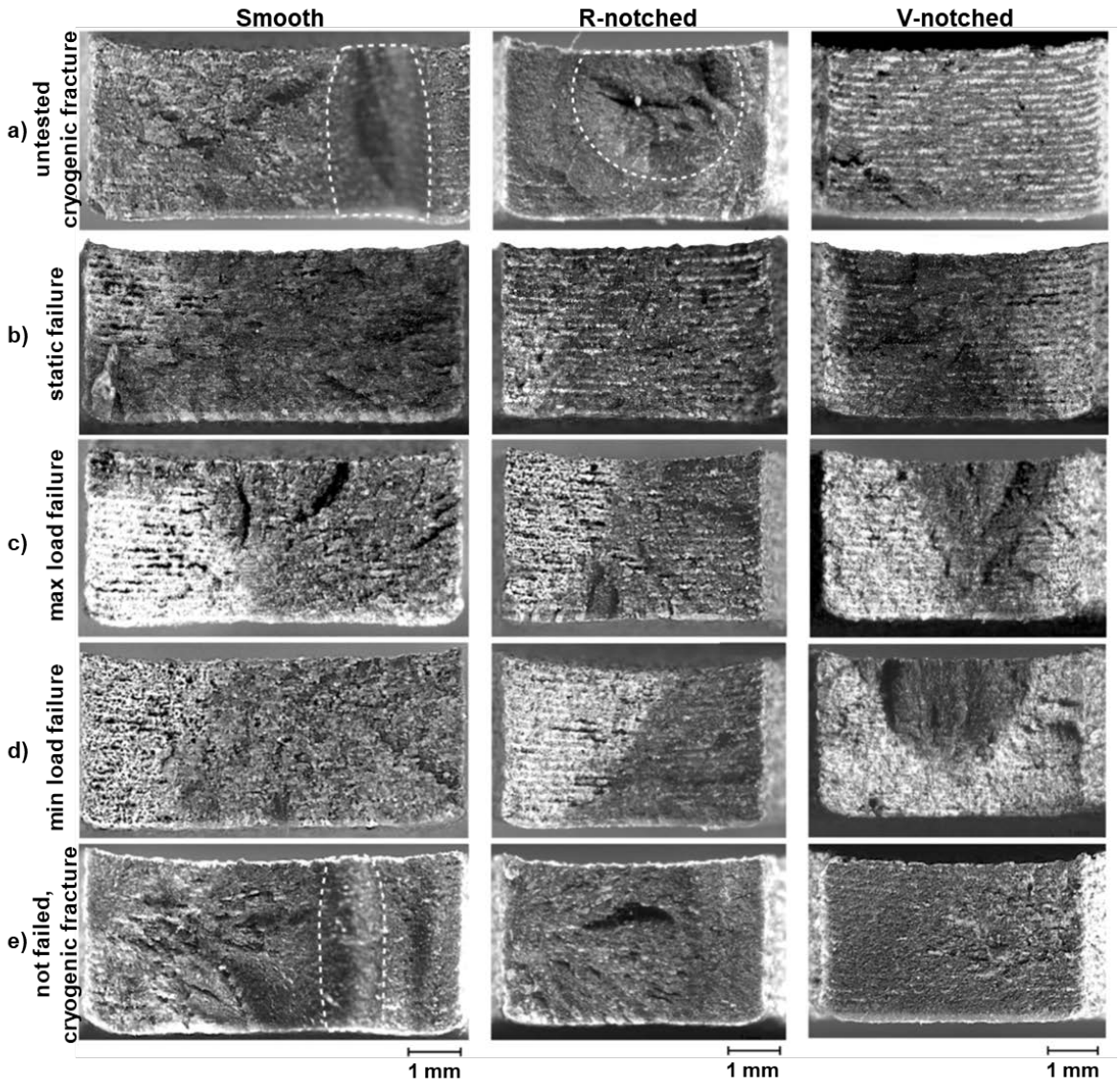

Fig. 8: Fracture surfaces for the three types of specimen under specific failure conditions: a) untested specimens fractured under cryogenic conditions; b) specimen failed under quasi-static conditions; c) specimen failed under fatigue at the maximum applied stress for each polymer (Smooth and R-notched: about 36 MPa; V-notched: about 31MPa); d) specimen failed under fatigue at the minimum applied stress for each polymer (Smooth and R-notched: about 29 MPa; V-notch: about 20MPa); e) specimen not failed under fatigue after 106 cycles and post-fractured under cryogenic conditions.

4. CONCLUSIONS

Multi Jet Fusion (MJF) is a very promising additive manufacturing process for industrial applications because of its suitability to produce large quantities of high-quality parts in reduced times. Extension to structural components could be hindered by lack of knowledge on its static and fatigue behavior and associated failure

CC BY NC ND

mechanisms, as well as on sensitivity to the presence of a notch. To this aim, in the present work, we provided new relevant data concerning these aspects:

- The mechanical performances of MJF-PA12 were comparable to those of PA12 manufactured with conventional methods in terms of Young's modulus and strength. The tensile stress-strain curve could be accurately fit with a Ramberg-Osgood type equation.
- Under quasi-static loading, for V-notched specimens, the experimental notch factor at failure K_{st} was much lower that the theoretical K_t. For the round notch this effect was less noticeable. Notch strengthening effects were not observed.
- Preliminary investigations show that TCD could be applicable to MJF-PA12 for failure prediction under quasi-static and fatigue loads but further tests with different notch geometry are necessary to assess the suitability of the model.
- The estimated fatigue strength for Smooth specimens was comparable to literature data on SLS-PA12 or injection molded PA12.
- Under cyclic loading, for V-notched specimens, the fatigue notch factor K_f was much lower that the theoretical K_t. For the round notch this effect was less noticeable. Notch strengthening effects were not observed. R-notched showed a fatigue notch sensitivity, q, close to zero, whereas a value of 0.159 could be estimated for the V-notched.

ACKNOWLEDGEMENTS

The authors would like to thank Antonio Vulcano and ELMEC 3d S.p.A for their support to the research by providing samples and information on the process.

AUTHORS' CONTRIBUTIONS

Conceptualization [Andrea Avanzini]; Methodology [Andrea Avanzini, Davide Battini, Stefano Pandini]; Investigation [Andrea Avanzini, Davide Battini, Stefano Pandini]; Resources [Andrea Avanzini, Stefano Pandini]; Writing - Original Draft [Andrea Avanzini, Davide Battini, Stefano Pandini]; Writing - Review & Editing [Andrea Avanzini, Davide Battini, Stefano Pandini]; Data Curation [Andrea Avanzini, Davide Battini, Stefano Pandini]; Visualization [Andrea Avanzini, Davide Battini, Stefano Pandini]

REFERENCES

[1] I.M. Kusoglu, C. Doñate-buendía, S. Barcikowski, B. Gökce, Laser powder bed fusion of polymers: Quantitative research direction indices, Materials (Basel). 14 (2021) 1–26. doi:10.3390/ma14051169.

[2] L.J. Tan, W. Zhu, K. Zhou, Recent Progress on Polymer Materials for Additive Manufacturing, Adv. Funct. Mater. 30 (2020) 1–54. doi:10.1002/adfm.202003062.

[3] C. Cai, W.S. Tey, J. Chen, W. Zhu, X. Liu, T. Liu, L. Zhao, K. Zhou, Comparative study on 3D printing of polyamide 12 by selective laser sintering and multi jet fusion, J. Mater. Process. Technol. 288 (2021) 116882. doi:10.1016/j.jmatprotec.2020.116882.

[4] H. Kim, Y. Zhao, L. Zhao, Process-level modeling and simulation for HP's Multi Jet Fusion 3D printing technology, 2016 1st Int. Work. Cyber-Physical Prod. Syst. CPPS 2016. (2016) 1–4. doi:10.1109/CPPS.2016.7483916.

[5] J.M. Jafferson, D. Chatterjee, A review on polymeric materials in additive manufacturing, Mater. Today Proc. 46 (2021) 1349–1365. doi:10.1016/j.matpr.2021.02.485.

[6] H.J. O'Connor, A.N. Dickson, D.P. Dowling, Evaluation of the mechanical performance of polymer parts fabricated using a production scale multi jet fusion printing process, Addit. Manuf. 22 (2018) 381–387. doi:10.1016/j.addma.2018.05.035.

[7] M. Schmid, K. Wegener, Additive Manufacturing: Polymers applicable for laser sintering (LS), Procedia Eng. 149 (2016) 457–464. doi:10.1016/j.proeng.2016.06.692.

[8] B. Lohfeld, Stefan; McHugh, Peter E.; Caulfield, Dependence of mechanical properties of polyamide components on build parameters in the SLS process, J. Mater. Process. Technol. (2007). doi:10.1016/j.matprotec.2006.09.007.

[9] E.C. Hofland, I. Baran, D.A. Wismeijer, Correlation of Process Parameters with Mechanical Properties of Laser Sintered PA12 Parts, Adv. Mater. Sci. Eng. 2017 (2017). doi:10.1155/2017/4953173.

[10] N. Saleh, N. Hopkinson, R.J.M. Hague, Investigating mechanical anisotropy and end-of-vector effect in laser-sintered nylon parts, Proc. IMechE Part B J. Eng. Manuf. 220 (2006) 1077–1086. doi:10.1243/09544054JEM537.

[11] J. Schneider, S. Kumar, Multiscale characterization and constitutive parameters identification of polyamide (PA12) processed via selective laser sintering, Polym. Test. 86 (2020) 106357. doi:10.1016/j.polymertesting.2020.106357.

[12] B. Van Hooreweder, D. Moens, R. Boonen, J.-P. Kruth, P. Sas, On the difference in material structure and fatigue properties of nylon specimens produced by injection molding and selective laser sintering, Polym. Test. 32 (2013) 972–981. doi:10.1016/j.polymertesting.2013.04.014.

[13] C.E. Majewski, H. Zarringhalam, N. Hopkinson, Effects of degree of particle melt and crystallinity in SLS Nylon-12 parts, 19th Annu. Int. Solid Free. Fabr. Symp. SFF 2008. (2008) 45–54.

[14] Z. Zhu, C. Majewski, Understanding pore formation and the effect on mechanical properties of High

CC BY NC ND

Speed Sintered polyamide-12 parts: A focus on energy input, Mater. Des. 194 (2020) 108937. doi:10.1016/j.matdes.2020.108937.

[15] ISO/ASTM52900-15, Standard Terminology for Additive Manufacturing – General Principles – Terminology (ASTM52900), Int. Organ. Stand. Geneva, Switz. i (2015) 1–9.

[16] D.L. Bourell, T.J. Watt, D.K. Leigh, B. Fulcher, Performance limitations in polymer laser sintering, Phys. Procedia. 56 (2014) 147–156. doi:10.1016/j.phpro.2014.08.157.

[17] M. Galati, F. Calignano, S. Defanti, L. Denti, Disclosing the build-up mechanisms of multi jet fusion: Experimental insight into the characteristics of starting materials and finished parts, J. Manuf. Process. 57 (2020) 244–253. doi:10.1016/j.jmapro.2020.06.029.

[18] Z. Xu, Y. Wang, D. Wu, K.P. Ananth, J. Bai, The process and performance comparison of polyamide 12 manufactured by multi jet fusion and selective laser sintering, J. Manuf. Process. 47 (2019) 419–426. doi:10.1016/j.jmapro.2019.07.014.

[19] S. Rosso, R. Meneghello, L. Biasetto, L. Grigolato, G. Concheri, G. Savio, In-depth comparison of polyamide 12 parts manufactured by Multi Jet Fusion and Selective Laser Sintering, Addit. Manuf. 36 (2020) 101713. doi:10.1016/j.addma.2020.101713.

[20] J. Riedelbauch, D. Rietzel, G. Witt, Analysis of material aging and the influence on the mechanical properties of polyamide 12 in the Multi Jet Fusion process, Addit. Manuf. 27 (2019) 259–266. doi:10.1016/j.addma.2019.03.002.

[21] P.V. Osswald, P. Obst, G.A. Mazzei Capote, M. Friedrich, D. Rietzel, G. Witt, Failure criterion for PA 12 multi-jet fusion additive manufactured parts, Addit. Manuf. 37 (2021) 101668. doi:10.1016/j.addma.2020.101668.

[22] B. Van Hooreweder, J.-P. Kruth, High cycle fatigue properties of selective laser sintered parts in polyamide 12, CIRP Ann. 63 (2014) 241–244. doi:10.1016/J.CIRP.2014.03.060.

[23] D. Santonocito, Evaluation of fatigue properties of 3D-printed Polyamide-12 by means of energy approach during tensile tests, Procedia Struct. Integr. 25 (2020) 355–363. doi:10.1016/j.prostr.2020.04.040.

[24] B. Van Hooreweder, F. De Coninck, D. Moens, R. Boonen, P. Sas, Microstructural characterization of SLS-PA12 specimens under dynamic tension/compression excitation, Polym. Test. 29 (2010) 319–326. doi:10.1016/J.POLYMERTESTING.2009.12.006.

[25] J. Munguia, K. Dalgarno, J. Munguia, K. Dalgarno, Fatigue behaviour of laser sintered Nylon 12 in rotating and reversed bending tests, Mater. Sci. Technol. 0836 (2015) 904–911. doi:10.1179/1743284715Y.0000000014.

[26] A.J. Cano, A. Salazar, J. Rodríguez, Effect of the orientation on the fatigue crack growth of polyamide 12 manufactured by selective laser sintering, Rapid Prototyp. J. 25 (2019) 820–829. doi:10.1108/RPJ-09-2018-0255.

[27] M. Crespo, T. Gómez-del Río, J. Rodríguez, Failure of polyamide 12 notched samples manufactured by selective laser sintering, J. Strain Anal. Eng. Des. 54 (2019) 192–198.

CC BY NC ND

doi:10.1177/0309324719847817.

[28] A. Zolfagharian, M.R. Khosravani, A. Kaynak, Fracture resistance analysis of 3D-printed polymers, Polymers (Basel). 12 (2020) 1–18. doi:10.3390/polym12020302.

[29] S.M.J.M.J. Razavi, P. Ferro, F. Berto, J. Torgersen, Fatigue strength of blunt V-notched specimens produced by selective laser melting of Ti-6Al-4V, Theor. Appl. Fract. Mech. 97 (2018) 376–384. doi:10.1016/j.tafmec.2017.06.021.

[30] S.M.J. Razavi, A. Avanzini, G. Cornacchia, L. Giorleo, F. Berto, Effect of heat treatment on fatigue behavior of as-built notched Co-Cr-Mo parts produced by Selective Laser Melting, Int. J. Fatigue. 142 (2021) 105926. doi:10.1016/j.ijfatigue.2020.105926.

[31] S. Gogolewski, K. Czerniawska, M. Gasiorek, Effect of annealing on thermal properties and crystalline structure of polyamides. Nylon 12 (polylaurolactam), 1136 (1980) 1130–1136.

[32] J. Zhang, A. Adams, Understanding thermal aging of non-stabilized and stabilized polyamide 12 using 1H solid-state NMR, Polym. Degrad. Stab. 134 (2016) 169–178. doi:10.1016/j.polymdegradstab.2016.10.006.

[33] HP, HP 3D Printing materials for the HP Jet Fusion 4200 3D Printing Solution, 2020.

[34] S. Morales-Planas, J. Minguella-Canela, J. Lluma-Fuentes, J.A. Travieso-Rodriguez, A.A. García-Granada, J. Antonio, Multi Jet Fusion PA12 manufacturing parameters for watertightness, strength and tolerances, Materials (Basel). 11 (2018) 1–11. doi:10.3390/ma11081472.

[35] F. Sillani, R.G. Kleijnen, M. Vetterli, M. Schmid, K. Wegener, Selective laser sintering and multi jet fusion: Process-induced modification of the raw materials and analyses of parts performance, Addit. Manuf. 27 (2019) 32–41. doi:10.1016/j.addma.2019.02.004.

[36] T. Palma, M. Munther, P. Damasus, S. Salari, A. Beheshti, K. Davami, Multiscale mechanical and tribological characterizations of additively manufactured polyamide 12 parts with different print orientations, J. Manuf. Process. 40 (2019) 76–83. doi:10.1016/j.jmapro.2019.03.004.

[37] N.E. Dowling, Mechanical behavior of materials, 2000.

[38] N. Lammens, M. Kersemans, I. De Baere, W. Van Paepegem, On the visco-elasto-plastic response of additively manufactured polyamide-12 (PA-12) through selective laser sintering, Polym. Test. 57 (2017) 149–155. doi:10.1016/j.polymertesting.2016.11.032.

[39] I. Sagradov, D. Schob, R. Roszak, P. Maasch, H. Sparr, M. Ziegenhorn, Experimental investigation and numerical modelling of 3D printed polyamide 12 with viscoplasticity and a crack model at different strain rates, Mater. Today Commun. 25 (2020) 101542. doi:10.1016/j.mtcomm.2020.101542.

[40] Srinivasulu K, N. Dhiraj Kumar, a Review on Properties of Surgical Sutures and Applications in Medical Field, IMPACT Int. J. Res. Eng. Technol. (IMPACT IJRET). 2 (2014) 85–96.

[41] K. Chen, H.W.B. Teo, W. Rao, G. Kang, K. Zhou, J. Zeng, H. Du, Experimental and modeling investigation on the viscoelastic-viscoplastic deformation of polyamide 12 printed by Multi Jet Fusion, Int. J. Plast. 143 (2021) 103029. doi:10.1016/j.ijplas.2021.103029.

[42] R. Louks, H. Askes, L. Susmel, Static assessment of brittle/ductile notched materials: An engineering

CC BY NC ND

approach based on the Theory of Critical Distances, Frat. Ed Integrita Strutt. 30 (2014) 23–30. doi:10.3221/IGF-ESIS.30.04.

[43] A.A. Ahmed, L. Susmel, A material length scale–based methodology to assess static strength of notched additively manufactured polylactide (PLA), Fatigue Fract. Eng. Mater. Struct. 41 (2018) 2071–2098. doi:10.1111/ffe.12746.

[44] R. Negru, L. Marsavina, T. Voiconi, E. Linul, H. Filipescu, G. Belgiu, Application of TCD for brittle fracture of notched PUR materials, Theor. Appl. Fract. Mech. 80 (2015) 87–95. doi:10.1016/j.tafmec.2015.05.005.

[45] C.T. Ng, L. Susmel, Notch static strength of additively manufactured acrylonitrile butadiene styrene (ABS), Addit. Manuf. 34 (2020) 101212. doi:10.1016/j.addma.2020.101212.

[46] A.A. Ahmed, L. Susmel, Static assessment of plain/notched polylactide (PLA) 3D-printed with different infill levels: Equivalent homogenised material concept and Theory of Critical Distances, Fatigue Fract. Eng. Mater. Struct. 42 (2019) 883–904. doi:10.1111/ffe.12958.

[47] O.H. Ezeh, L. Susmel, On the notch fatigue strength of additively manufactured polylactide (PLA), Int. J. Fatigue. 136 (2020) 105583. doi:10.1016/j.ijfatigue.2020.105583.

[48] D. Taylor, The theory of critical distances applied to the prediction of brittle fracture in metallic materials, SID Struct. Integr. Durab. 1 (2005) 145–154. doi:10.3970/sdhm.2005.001.145.

[49] L. Susmel, D. Taylor, The Theory of Critical Distances as an alternative experimental strategy for the determination of KIc and ΔKth, Eng. Fract. Mech. 77 (2010) 1492–1501. doi:10.1016/j.engfracmech.2010.04.016.

[50] A. Salazar, A. Rico, J. Rodríguez, J. Segurado Escudero, R. Seltzer, F. Martin De La Escalera Cutillas, Fatigue crack growth of SLS polyamide 12: Effect of reinforcement and temperature, Compos. Part B Eng. 59 (2014) 285–292. doi:10.1016/j.compositesb.2013.12.017.

[51] D.I. Stoia, L. Marsavina, E. Linul, Mode I fracture toughness of polyamide and alumide samples obtained by selective laser sintering additive process, Polymers (Basel). 12 (2020). doi:10.3390/polym12030640.

[52] F. Calignano, F. Giuffrida, M. Galati, Effect of the build orientation on the mechanical performance of polymeric parts produced by multi jet fusion and selective laser sintering, J. Manuf. Process. 65 (2021) 271–282. doi:10.1016/j.jmapro.2021.03.018.

[53] A. Avanzini, G. Donzella, D. Gallina, S. Pandini, C. Petrogalli, Fatigue behavior and cyclic damage of peek short fiber reinforced composites, Compos. Part B Eng. 45 (2013) 397–406. doi:10.1016/j.compositesb.2012.06.008.

[54] S. Mortazavian, A. Fatemi, Fatigue behavior and modeling of short fiber reinforced polymer composites: A literature review, Int. J. Fatigue. 70 (2015) 297–321. doi:10.1016/j.ijfatigue.2014.10.005.

[55] Z. Lu, B. Feng, C. Loh, Fatigue behaviour and mean stress effect of thermoplastic polymers and composites, Frat. Ed Integrita Strutt. 12 (2018) 150–157. doi:10.3221/IGF-ESIS.46.15.

CC BY NC ND

[56] S. Mortazavian, A. Fatemi, Effects of mean stress and stress concentration on fatigue behavior of short fiber reinforced polymer composites, Fatigue Fract. Eng. Mater. Struct. 39 (2016) 149–166. doi:10.1111/ffe.12341.

[57] O.H. Ezeh, L. Susmel, Fatigue strength of additively manufactured polylactide (PLA): effect of raster angle and non-zero mean stresses, Int. J. Fatigue. 126 (2019) 319–326. doi:10.1016/j.ijfatigue.2019.05.014.

[58] S.M.J. Razavi, F. Berto, Directed Energy Deposition versus Wrought Ti-6Al-4V: A Comparison of Microstructure, Fatigue Behavior, and Notch Sensitivity, Adv. Eng. Mater. 1900220 (2019) 1–15. doi:10.1002/adem.201900220.

[59] K. Solberg, F. Berto, Notch-defect interaction in additively manufactured Inconel 718, Int. J. Fatigue. 122 (2019) 35–45. doi:10.1016/j.ijfatigue.2018.12.021.

[60] S. Mortazavian, A. Fatemi, Notch Effects on Fatigue Behavior of Thermoplastics, Adv. Mater. Res. 891–892 (2014) 1403–1409. doi:10.4028/www.scientific.net/AMR.891-892.1403.

[61] L. Susmel, The Theory of Critical Distances: Applications in Fatigue, in: Fract. Nano Eng. Mater. Struct., Springer Netherlands, Dordrecht, 2006: pp. 1101–1102. doi:10.1007/1-4020-4972-2_546.

[62] A. Avanzini, D. Gallina, Effect of Cyclic Strain on the Mechanical Behavior of a Thermoplastic Polyurethane, J. Eng. Mater. Technol. 133 (2011) 021005. doi:10.1115/1.4003101.

[63] A. Avanzini, Effect of cyclic strain on the mechanical behavior of virgin ultra-high molecular weight polyethylene, J. Mech. Behav. Biomed. Mater. 4 (2011) 1242–1256. doi:10.1016/j.jmbbm.2011.04.010.

[64] D. Hülsbusch, A. Kohl, P. Striemann, M. Niedermeier, J. Strauch, F. Walther, Development of an energy-based approach for optimized frequency selection for fatigue testing on polymers – Exemplified on polyamide 6, Polym. Test. 81 (2020) 106260. doi:10.1016/j.polymertesting.2019.106260.

[65] A. Avanzini, C. Petrogalli, D. Battini, G. Donzella, Influence of micro-notches on the fatigue strength and crack propagation of unfilled and short carbon fiber reinforced PEEK, Mater. Des. 139 (2018) 447–456. doi:10.1016/j.matdes.2017.11.039.

CC BY NC ND